RESEARCH ARTICLE

CARBON ENERGY WILEY

3D-cavity-confined CsPbBr₃ quantum dots for visible-light-driven photocatalytic C(sp³)–H bond activation

Yu-Jie Gao[1] | Handong Jin[2] | Daniel A. Esteban[3] | Bo Weng[1] |
Rafikul A. Saha[1] | Min-Quan Yang[4] | Sara Bals[3] | Julian A. Steele[1,5,6] |
Haowei Huang[1] | Maarten B. J. Roeffaers[1]

[1]Centre for Membrane Separations, Adsorption, Catalysis and Spectroscopy for Sustainable Solutions (cMACS), KU Leuven, Leuven, Belgium

[2]Department of Chemistry, KU Leuven, Leuven, Belgium

[3]Electron Microscopy for Materials Science (EMAT), University of Antwerp, Antwerpen, Belgium

[4]Fujian Key Laboratory of Pollution Control and Resource Reuse, College of Environmental and Resource Sciences, College of Carbon Neutral Modern Industry, Fujian Normal University, Fuzhou, China

[5]Australian Institute for Bioengineering and Nanotechnology, The University of Queensland, Brisbane, Queensland, Australia

[6]School of Mathematics and Physics, The University of Queensland, Brisbane, Queensland, Australia

Correspondence
Bo Weng, Haowei Huang, and Maarten B. J. Roeffaers, Centre for Membrane Separations, Adsorption, Catalysis and Spectroscopy for Sustainable Solutions (cMACS), KU Leuven, Celestijnenlaan 200F, 3001 Leuven, Belgium.
Email: bo.weng@kuleuven.be, haowei.huang@kuleuven.be and maarten.roeffaers@kuleuven.be

Abstract

Metal halide perovskite (MHP) quantum dots (QDs) offer immense potential for several areas of photonics research due to their easy and low-cost fabrication and excellent optoelectronic properties. However, practical applications of MHP QDs are limited by their poor stability and, in particular, their tendency to aggregate. Here, we develop a two-step double-solvent strategy to grow and confine CsPbBr₃ QDs within the three-dimensional (3D) cavities of a mesoporous SBA-16 silica scaffold (CsPbBr₃@SBA-16). Strong confinement and separation of the MHP QDs lead to a relatively uniform size distribution, narrow luminescence, and good ambient stability over 2 months. In addition, the CsPbBr₃@SBA-16 presents a high activity and stability for visible-light-driven photocatalytic toluene C(sp³)–H bond activation to produce benzaldehyde with ~730 μmol g^{-1} h^{-1} yield rate and near-unity selectivity. Similarly, the structural stability of CsPbBr₃@SBA-16 QDs is superior to that of both pure CsPbBr₃ QDs and those confined in MCM-41 with 1D channels.

KEYWORDS
3D cavity silica, C(sp³)–H bond activation, perovskite quantum dots, photocatalysis, stability

INTRODUCTION

The production of value-added products using abundant industrial feedstocks is always highly desirable in organic synthesis. A classic paradigm is utilizing directly $C(sp^3)$–H functionalization to convert petroleum-derived toluene and its derivatives into valuable oxygenated compounds. However, due to the low thermodynamic reactivity and high bond dissociation energy ($88.5 \pm 1.5 \, \text{kcal} \times \text{mol}^{-1}$) of $C(sp^3)$–H bonds in toluene, the $C(sp^3)$–H functionalization reaction generally demands harsh reaction conditions (e.g., high temperature, pressure, or corrosive reagents), leading to adverse environmental impacts as well as high energy costs.[1] Semiconductor photocatalysis provides a promising solution to utilize solar energy to overcome the large energy barrier of C–H bond activation. However, the reported photocatalysts, until now, fall short of the ideal, suffering from wide bandgaps, low charge separation efficiencies, and poor product selectivity (resulting from overoxidation). Metal halide perovskites (MHPs) are highly promising photocatalysts due to their tunable bandgap, long carrier diffusion length and lifetime, and easy and low-cost fabrication.[2–4] Recently, MHP photocatalysts have been developed remarkably in CO_2 reduction and H_2 evolution.[5–9] Furthermore, their photocatalytic performance in organic synthesis and dye degradation has proven to be highly promising.[2,5,6,10] Perovskite quantum dots (PQDs) are of particular interest because of their stronger redox power and abundant active surface sites, which improve photocatalytic properties from their bulk counterparts.[2,3,5–14] However, the traditional PQDs fabrication approaches, such as hot injection and antisolvent, require long-chain organic surfactants that cover the surface of QDs, decreasing their interaction with reactants during photocatalytic reactions.[3,15,16] Additionally, the PQDs generally suffer from degradation and/or aggregation under sustained photocatalytic conditions (such as light, water, and oxygen) due to water-induced hydration of PQDs or radical-promoted removal of surface ligands. These disadvantages hinder the photocatalytic applications of PQDs.[3,6,11,17,18]

Recently, a template-assisted PQD fabrication method has been proposed, which uses physical restriction inside a template material's pores to control the MHP size.[11,19] Importantly, this method does not need surfactants to prepare PQDs and hence offers the ability of freely available surfaces, which is important for reactant adsorption during photocatalytic reactions.[2,7,20] Mesoporous silicas with tunable pore sizes (from 2 to 50 nm), periodic mesoporous structure, and a large pore volume are excellent candidates as template materials to control MHP size.[2,7,12,19,21–27] So far, the template-assisted growth of PQDs inside mesoporous silicas has been limited to materials with one-dimensional (1D) channels.[2,7,12,19,21–28] Unfortunately, due to the mobility of

MHPs, these 1D channels are not very effective in stabilizing PQDs.[22,23] To enhance PQD stability, the 1D channels of the template material are typically further sealed or closed, which is undesirable in photocatalysis because it renders PQDs inaccessible to reaction substrates.[23,27]

In this study, we have exploited the 3D spherical cavities (6.2 nm) connected via small windows (3.4 nm) of SBA-16 as a template to effectively assist the formation of PQDs and stabilize them while also keeping them accessible to chemicals/small molecules. To effectively confine the PQDs inside SBA-16, the hydrophilic difference between the inner and outer surface of SBA-16 was exploited in a novel two-step double-solvent (TSDS) strategy. The PQDs exhibit a uniform size of ~4.3 nm. As a result, the $CsPbBr_3$@SBA-16 displays a narrow luminescence emission with a full width at half maximum (FWHM) of only 18 nm (0.087 eV). Furthermore, when used as a photocatalyst in the visible-light-driven photocatalytic toluene $C(sp^3)$–H bond activation, the $CsPbBr_3$@SBA-16 shows the best stability compared to surfactant-stabilized $CsPbBr_3$ QDs and 1D channel-templated $CsPbBr_3$ QDs ($CsPbBr_3$@MCM-41) and outstanding catalytic performance with a high conversion rate up to ~730 $\mu\text{mol g}^{-1}\,\text{h}^{-1}$. Additionally, the stability of these cavity-confined $CsPbBr_3$ PQDs is greatly improved in comparison to those confined in the 1D channels of MCM-41. After exposure to ambient conditions for more than 2 months, $CsPbBr_3$@SBA-16 preserves its structure and optoelectronic properties.

RESULTS AND DISCUSSIONS

Traditional techniques to confine perovskites into the pores of template materials generally include solution infiltration and solid grinding, bringing difficulties to completely remove the perovskites precursor, leading to the unwanted formation of bulk perovskites on the external surface of template material.[2,24] To ensure the effective formation of only cavity-confined PQDs, a TSDS strategy was developed, as illustrated in Figure 1A. First, commercial SBA-16 with a cavity size of 6.2 nm and window size of 3.4 nm was suspended in hexane. To this suspension, a more hydrophilic CsBr dimethyl sulfoxide (DMSO) solution (0.2 M, $V_{\text{solution}} = 1/2V_{\text{pore of SBA-16}}$) is added. In this way, the CsBr is effectively introduced into the cavities. Next, a stoichiometric amount of $PbBr_2$ in DMSO (0.2 M, $V_{\text{solution}} = 1/2V_{\text{pore of SBA-16}}$) is added to this CsBr-loaded SBA-16 suspension in hexane; both steps are performed under vigorous stirring. Due to the hydrophilic inner surface of SBA-16, these two DMSO salt solutions are forced into the cavity by capillary force. The hexane was removed by filtration, and the remaining DMSO was removed through heating to obtain $CsPbBr_3$@SBA-16. For
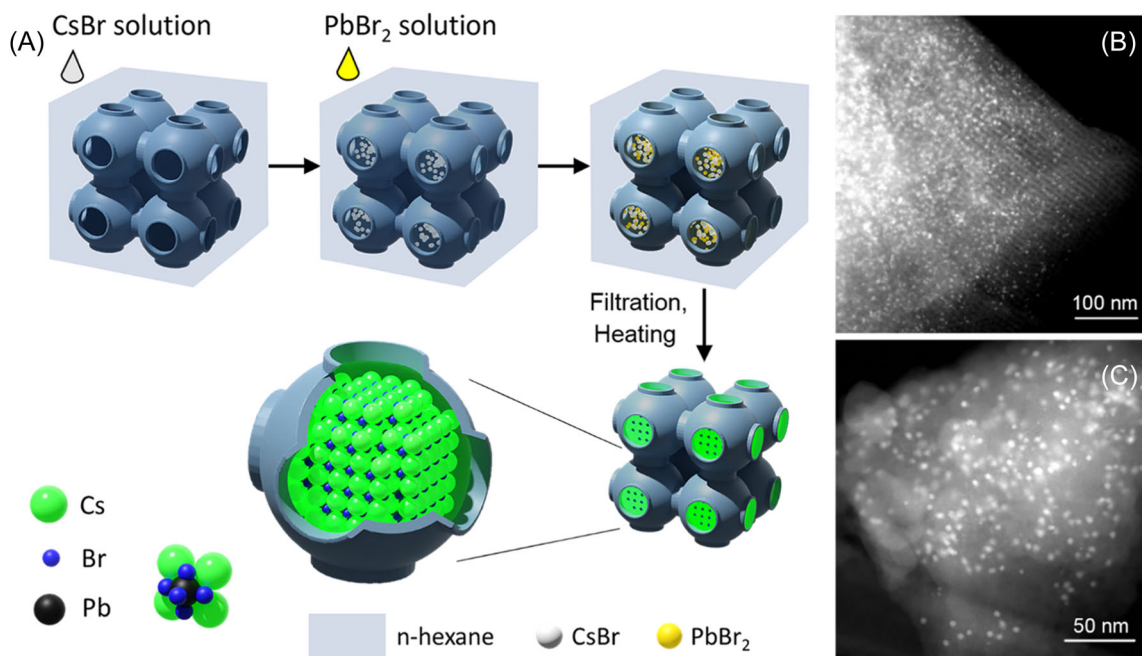
FIGURE 1 (A) Schematic diagram of the fabrication of CsPbBr$_3$ in the cavities of mesoporous silica SBA-16 using the two-step double-solvent strategy. (B, C) HAADF-STEM images of CsPbBr$_3$@SBA-16.

comparison, we used the same synthesis approach to prepare CsPbBr$_3$ with the 1D channels of MCM-41 (CsPbBr$_3$@MCM-41) and nonporous SiO$_2$ (CsPbBr$_3$/np-SiO$_2$). N$_2$-physisorption isotherm and pore size distribution analysis revealed different pore types for the 3D cavity template SBA-16 and the 1D channel template MCM-41 (Figures S1 and S2).

X-ray diffraction (XRD) patterns in Figure S3 indicate that the characteristic diffraction peaks of orthorhombic CsPbBr$_3$ are only detected in the CsPbBr$_3$/np-SiO$_2$ composite, as confirmed by the Rietveld refinement, but are absent in both CsPbBr$_3$@SBA-16 and CsPbBr$_3$@MCM-41, indicating that the very small PQDs were all confined in the nanoporous silica templates. Scanning electron microscopy (SEM) images and the elemental mapping of the CsPbBr$_3$/np-SiO$_2$ composite in Figure S4 show that the bulk CsPbBr$_3$ particles with sizes ranging from 0.2 to 0.6 μm were formed on the surface of np-SiO$_2$. In contrast, CsPbBr$_3$@SBA-16 and CsPbBr$_3$@MCM-41 exhibit morphologies very similar to pure SBA-16 or MCM-41, with no CsPbBr$_3$ particles deposited on the external surfaces (Figures S5 and S6). This further suggests that CsPbBr$_3$ QDs may be located inside the silica templates. To confirm the presence of small CsPbBr$_3$ confined to the SBA-16 cavities and MCM-41 channels, high-angle annular dark-field scanning transmission electron microscopy (HAADF-STEM) was performed. As shown in Figures 1B,C and S7, small CsPbBr$_3$ QDs with a size of 4.3 ± 0.5 nm were well separated in the ordered cavities of SBA-16. In addition to 2D HAADF-STEM projection

images, tilt series of HAADF-STEM images were acquired for pure SBA-16 and CsPbBr$_3$@SBA-16 composite. 3D visualizations of the obtained electron tomography reconstructions demonstrated the 3D-ordered cavities of SBA-16 silica (Figure S8A and Video S1) and the successful confinement of CsPbBr$_3$ QDs in the cavities (Figures S8B and Video S2). Furthermore, STEM-dispersive X-ray (EDX) elemental mapping of the CsPbBr$_3$@SBA-16 composite was conducted to further confirm the presence of the CsPbBr$_3$ QDs in the cavities of SBA-16 (Figure S9). HAADF-STEM images and electron tomography also confirmed the effective formation of 2.3 ± 0.5 nm CsPbBr$_3$ QDs inside the channels of MCM-41 by the same TSDS method (Figures S10 and S11, Videos S3 and S4). Notably, no bulk CsPbBr$_3$ was observed at the surface of both mesoporous silicas, as further revealed by the orthoslices of the 3D reconstructions (Figure S12), indicating that the TSDS strategy is a facile and general synthesis method for all-inorganic PQDs. The structural schematic diagrams of CsPbBr$_3$@SBA-16, CsPbBr$_3$@MCM-41, and CsPbBr$_3$/np-SiO$_2$ are illustrated in Figure 2A. The content of CsPbBr$_3$ in these three samples was determined to be 2.15% by SEM-EDX (Table S1).

The N$_2$-physisorption isotherms were recorded on the SBA-16 sample before and after CsPbBr$_3$ (Figure S13). SBA-16 and CsPbBr$_3$@SBA-16 exhibited type IV isotherms with an H$_2$-type hysteresis loop, and the hysteresis loop shifted to relatively low pressure after introducing the CsPbBr$_3$ QDs. Compared to pure SBA-16, the obvious decrease from 598 to 393 m^{2}g^{-1} in the
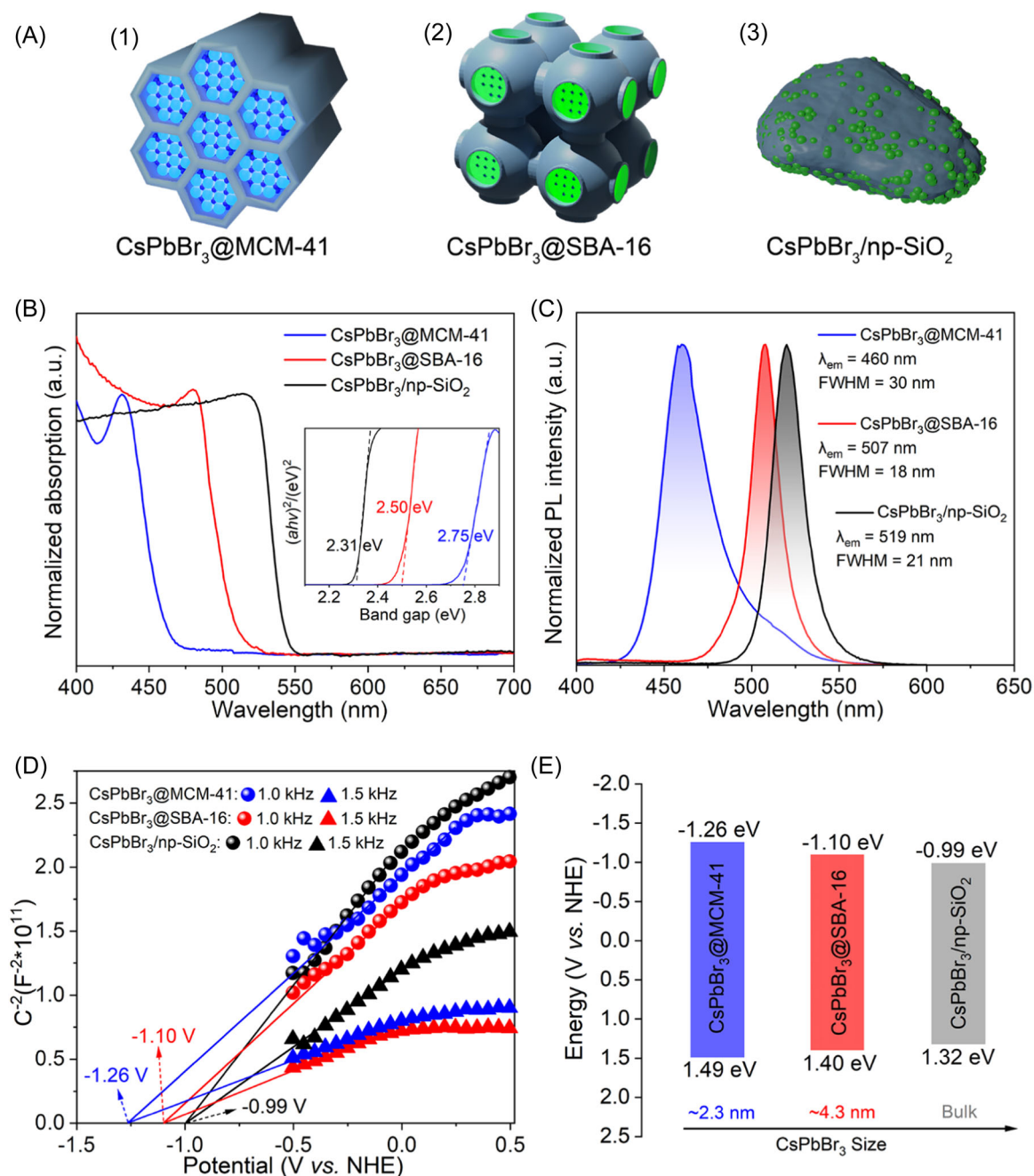
FIGURE 2 (A) Structural schematic diagrams illustrating the integration of $CsPbBr_3$ in three different matrices: (1) encapsulation within the mesoporous channels of MCM-41, denoted as $CsPbBr_3$@MCM-41; (2) incorporation into the internal cavities of SBA-16, represented as $CsPbBr_3$@SBA-16; and (3) deposition on the external surface of nonporous SiO_2, referred to as $CsPbBr_3$/np-SiO_2. (B) UV–vis absorption spectra of these materials, with Tauc-plot curves presented in the inset, illustrating their optical properties. (C) PL spectra, showing the emission characteristics. (D) Mott–Schottky plots, providing insights into their electronic properties. (E) Band structures derived from the data in (B–D), highlighting the electronic band positions of the different $CsPbBr_3$-based nanocomposites.

Brunauer–Emmett–Teller surface area and decrease from 0.42 to 0.32 $cm^3 g^{-1}$ in the pore volume were observed over $CsPbBr_3$@SBA-16, which was caused by the incorporation of $CsPbBr_3$ QDs within the SBA-16 cavities (Table S2). It is interesting to note that the confined $CsPbBr_3$ crystal led to the decrease of cavity size from 6.2 to 5.5 nm, while the size of the pore entrance remained constant at 3.4 nm.

These findings indicate that $CsPbBr_3$ QDs are formed inside SBA-16 cavities rather than at the cavity entrances. The presence of these QDs reduces the volume available for N_2 adsorption, leading to an apparent decrease in cavity size. This confinement within the cavities is crucial for the formation of stable $CsPbBr_3$ QDs. In addition, the size of $CsPbBr_3$ QDs observed through transmission electron

microscopy, which is smaller than that of the cavity, indicates that CsPbBr$_3$ QD partially occupies the cavity within SBA-16.[29]

Next, the photophysical properties of CsPbBr$_3$@SBA-16, CsPbBr$_3$@MCM-41, and CsPbBr$_3$/np-SiO$_2$ composites were studied. CsPbBr$_3$@SBA-16 and CsPbBr$_3$@MCM-41 samples have a yellow color, while CsPbBr$_3$/np-SiO$_2$ has a more orange appearance (Figure S14). Figure 2B shows the ultraviolet–visible (UV–vis) absorption spectra for these three composites. The absorption edge of CsPbBr$_3$/np-SiO$_2$ is at ~537 nm, which corresponds to the reported bandgap of bulk CsPbBr$_3$ at about 2.31 eV.[15,30] The absorption edges of CsPbBr$_3$@SBA-16 and CsPbBr$_3$@MCM-41 are strongly blue-shifted to 500 and 451 nm, respectively. Correspondingly, the bandgaps of CsPbBr$_3$ in CsPbBr$_3$@SBA-16 and CsPbBr$_3$@MCM-41 are 2.50 and 2.75 eV, respectively, with a shift of 0.19 and 0.44 eV compared to that of the bulk CsPbBr$_3$. These larger bandgaps can be attributed to the quantum confinement in CsPbBr$_3$ PQDs with sizes smaller than the reported Bohr radius of ~7 nm for CsPbBr$_3$.[15] It is evident that the quantum confinement effect causes a decrease in solar light absorption. Based on the bandgap, we estimate the relative amounts of solar energy available with respect to bulk CsPbBr$_3$, that is, CsPbBr$_3$/np-SiO$_2$, to being 0.84 and 0.64 for CsPbBr$_3$@SBA-16 and CsPbBr$_3$@MCM-41, respectively. However, the reduction in particle size also results in a strong increase in the available surface areas, which are estimated to be 93 and 174 times larger for CsPbBr$_3$@SBA-16 and CsPbBr$_3$@MCM-41, respectively, compared to CsPbBr$_3$/np-SiO$_2$. Interestingly, the band edge exciton peak tended to be more prominent with the decreasing size of CsPbBr$_3$, indicating a stronger electron–hole correlation caused by the quantum confinement effect.[25,31,32] The steady-state photoluminescence (PL) spectra of CsPbBr$_3$@SBA-16, CsPbBr$_3$@MCM-41, and CsPbBr$_3$/np-SiO$_2$ are in line with these observations (Figure 2C). The CsPbBr$_3$/np-SiO$_2$ composite exhibits a PL maximum around 519 nm, and the PL emissions of CsPbBr$_3$@SBA-16 and CsPbBr$_3$@MCM-41 are, respectively, 12 and 59 nm blue-shifted. Figure S14 shows the visible PL emission of CsPbBr$_3$@SBA-16 (bright green), CsPbBr$_3$@MCM-41 (blue), and CsPbBr$_3$/np-SiO$_2$ (dark green) under 366 nm UV light excitation. The PL quantum yields (PLQY) of CsPbBr$_3$@SBA-16 and CsPbBr$_3$@MCM-41 reached 40% and 8%, respectively, much higher than that of CsPbBr$_3$/np-SiO$_2$ being 0.6%. Notably, the PL of CsPbBr$_3$@SBA-16 is ultranarrow with an FWHM of only 18 nm (0.087 eV), which is much better than that of CsPbBr$_3$@MCM-41 (30 nm, 0.176 eV), CsPbBr$_3$/np-SiO$_2$ (21 nm, 0.097 eV), and PQDs synthesized via reported template-assisted methods.[16,21,22,24,25,27] This is another support of the monodisperse nature of the CsPbBr$_3$ PQDs

confined within the SBA-16 cavities through the TSDS method. This uniformity in size distribution may lead to more consistent optical and electronic properties for the CsPbBr$_3$@SBA-16. In contrast, the CsPbBr$_3$/SBA-16 composite, which was prepared through the traditional template-assisted method, displays two bandgaps and a broad PL peak, indicating the formation of bulk perovskites on the surface (Figure S15B). These results demonstrated that the TSDS method is a facile and efficient strategy to confine PQDs in porous templates and avoid their aggregation on the surface.

Mott–Schottky measurements were employed to determine the conduction band edge of CsPbBr$_3$@SBA-16, CsPbBr$_3$@MCM-41, and CsPbBr$_3$/np-SiO$_2$ at 1.0 and 1.5 kHz, as depicted in Figure 2D. The Mott–Schottky slopes of all three samples are positive in the linear plot region, indicative of an n-type semiconductor.[33] According to the corresponding intercepts of the linear plot region with the potential axis of Mott–Schottky plots, the flat band potentials of CsPbBr$_3$/np-SiO$_2$, CsPbBr$_3$@SBA-16, and CsPbBr$_3$@MCM-41 were determined to be −0.99, −1.10, and −1.26 V versus the normal hydrogen electrode recorded at both 1.0 and 1.5 kHz, respectively. Bulk CsPbBr$_3$ film was also measured, and the flat band potential was as same as that of CsPbBr$_3$/np-SiO$_2$ (Figure S16). Since the conduction band edge potential of n-type semiconductors is practically associated with the flat band potential and the corresponding valence band edge potentials could be derived from their bandgaps, the band structures of all three CsPbBr$_3$ are illustrated in Figure 2E. Compared to bulk CsPbBr$_3$ on np-SiO$_2$, the small-size CsPbBr$_3$ QDs confined in SBA-16 and MCM-41 show a more positive valence band position and hence a stronger oxidation potential. This enhanced oxidation potential is crucial for photocatalytic reactions like toluene oxidation.

To test whether CsPbBr$_3$@SBA-16 has a superior photocatalytic activity and stability in comparison to CsPbBr$_3$@MCM-41, we employed these materials as photocatalysts for the selective photo-oxidation of C(sp^3)–H of the methyl group in toluene saturated with O$_2$ and visible light driven ($\lambda \geq 420$ nm) at room temperature.[34–36] As shown in Figure 3A, after 4 h visible-light illumination, CsPbBr$_3$@MCM-41 and CsPbBr$_3$@SBA-16 have the benzaldehyde (BAD) production rate of 348 and 527 μmol g^{-1} h^{-1}, respectively, and 100% selectivity. The blank experiment showed that no products were detected from the pure silica matrix. Additionally, we carried out a control experiment using BAD as the substrate in a trifluorotoluene solvent, saturated with oxygen, and employing CsPbBr$_3$@SBA-16 as the catalyst under visible light irradiation. After 4 h, benzyl alcohol, benzoin, or hydrogenated benzoin were not detected in the reaction
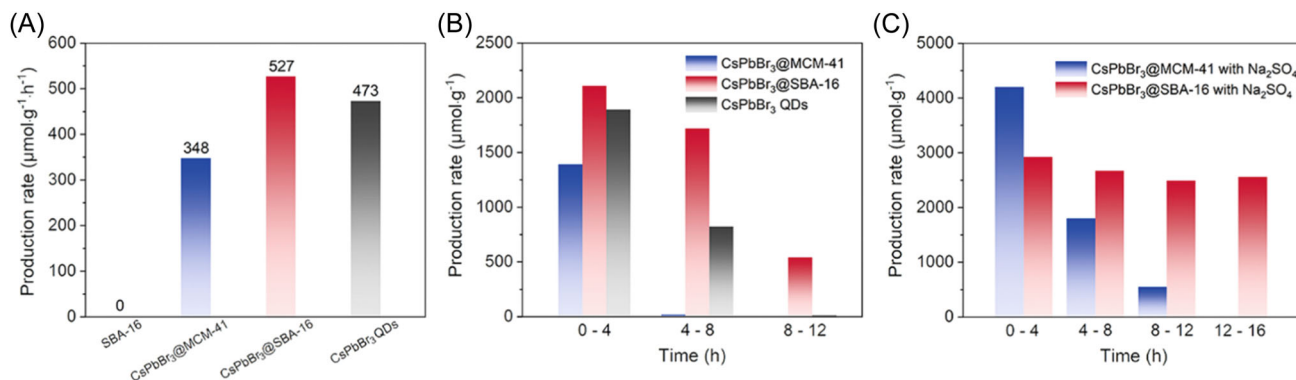
FIGURE 3 (A) Selective photocatalytic oxidation of pure toluene to benzaldehyde; conditions: 4 h irradiation (≥420 nm), the amount of $CsPbBr_3$ was kept constant 454 μg/2.5 mL reaction mixture. (B) The benzaldehyde production per 4 h over $CsPbBr_3$@MCM-41, $CsPbBr_3$@SBA−16, and pure $CsPbBr_3$ QDs. (C) The benzaldehyde production per 4 h over $CsPbBr_3$@MCM-41 and $CsPbBr_3$@SBA-16 by adding anhydrous Na_2SO_4.

mixture. As a reference, traditional ligand-contained $CsPbBr_3$ QDs were prepared and showed a BAD generation rate of 473 $\mu mol\,g^{-1}\,h^{-1}$. However, as shown in Figure 3B, the BAD production rate for ligand-contained $CsPbBr_3$ QDs slowed down after 4 h, and the reaction completely stopped within 8 h. Moreover, the $CsPbBr_3$@MCM-41 lost its activity in 4 h. In contrast, $CsPbBr_3$@SBA-16 presented relative stability, although the rate of BAD production gradually decreased during the 12 h reaction. The slowdown of the production rate may be due to the damage of the perovskite caused by the generated water, which is absorbed by the hydrophilic SBA-16.[30] The damage of MHP QDs can be prevented by the addition of anhydrous Na_2SO_4. As seen in Figure 3C, with anhydrous Na_2SO_4, the BAD production rate over $CsPbBr_3$@SBA-16 reached 730 $\mu mol\,g^{-1}\,h^{-1}$. After continuous reaction for 16 h, $CsPbBr_3$@SBA-16 exhibited remarkable stability by retaining 91% (665 $\mu mol\,g^{-1}\,h^{-1}$) of its initial activity. Despite the strong water-absorbing capacity of anhydrous Na_2SO_4, it was challenging to entirely eliminate the impact of generated water on $CsPbBr_3$. The visible light photocatalytic performance of $CsPbBr_3$@SBA-16 for $C(sp^3)$–H activation surpasses that of the majority of photocatalysts documented to date, as evidenced in Table S3. Notably, after 16 h of irradiation, a small amount of benzyl alcohol can be detected (Figure S17), while no other side products were detected in the reaction system. HAADF-STEM images after the long-time reaction revealed that $CsPbBr_3$ QDs were still trapped in the cavities of SBA-16 but outside of the channels of MCM-41 (Figure S18). Correspondingly, no leaching of Cs and Pd was detected in the reaction mixture by inductively coupled plasma analysis after a long-time photocatalytic reaction, further supporting the observed stability of $CsPbBr_3$@SBA-16. The absorption edge and PL peak of $CsPbBr_3$@SBA-16 remained constant after the

long-time reaction (Figure S19), indicating that the size of $CsPbBr_3$ QDs was almost unchanged. The absorption spectra of both ligand-contained $CsPbBr_3$ QDs and $CsPbBr_3$@MCM-41 changed obviously due to the aggregation and decomposition of QDs (Figure S20). These results demonstrate that the confinement of perovskite into 3D-cavity mesoporous silica is an efficient method to enhance the stability of perovskite QDs for photocatalytic applications.

To investigate the photocatalytic reaction mechanism involved in activating the $C(sp^3)$–H bond within the methyl group of toluene, a series of controlled experiments was carried out under various conditions. In our experiment, as depicted in Figure 4A, we introduced specific scavengers into the reaction system to target different reactive species: ammonium oxalate (AO) for holes (h^+), potassium persulfate ($K_2S_2O_8$) for electrons (e^-), 1,4-benzoquinone (BQ) for superoxide radicals ($\bullet O_2^-$), and t-butanol (TBA) for hydroxyl radicals ($\bullet OH$). First, upon introducing AO as an h^+ scavenger, toluene conversion was nearly completely suppressed, and the produced BAD fell between the limit of detection (LOD) and the limit of quantification (LOQ) of gas chromatography (GC). Second, with $K_2S_2O_8$ as an e^- scavenger, a substantial inhibition of toluene conversion was observed, affirming the importance of photogenerated electrons in the photocatalytic oxidation process. Despite this inhibition, a moderate yield of BAD was still achieved. Third, under an argon (Ar) atmosphere, where O_2 is absent, a significant decrease in toluene conversion was observed, emphasizing the indispensability of O_2 for the formation of oxygenated compounds. The residual conversion in the absence of O_2 is attributed to trace amounts of unmoved O_2. A similar effect was observed when BQ was introduced as a scavenger for $\bullet O_2^-$, affirming that $\bullet O_2^-$ radicals play a crucial role as

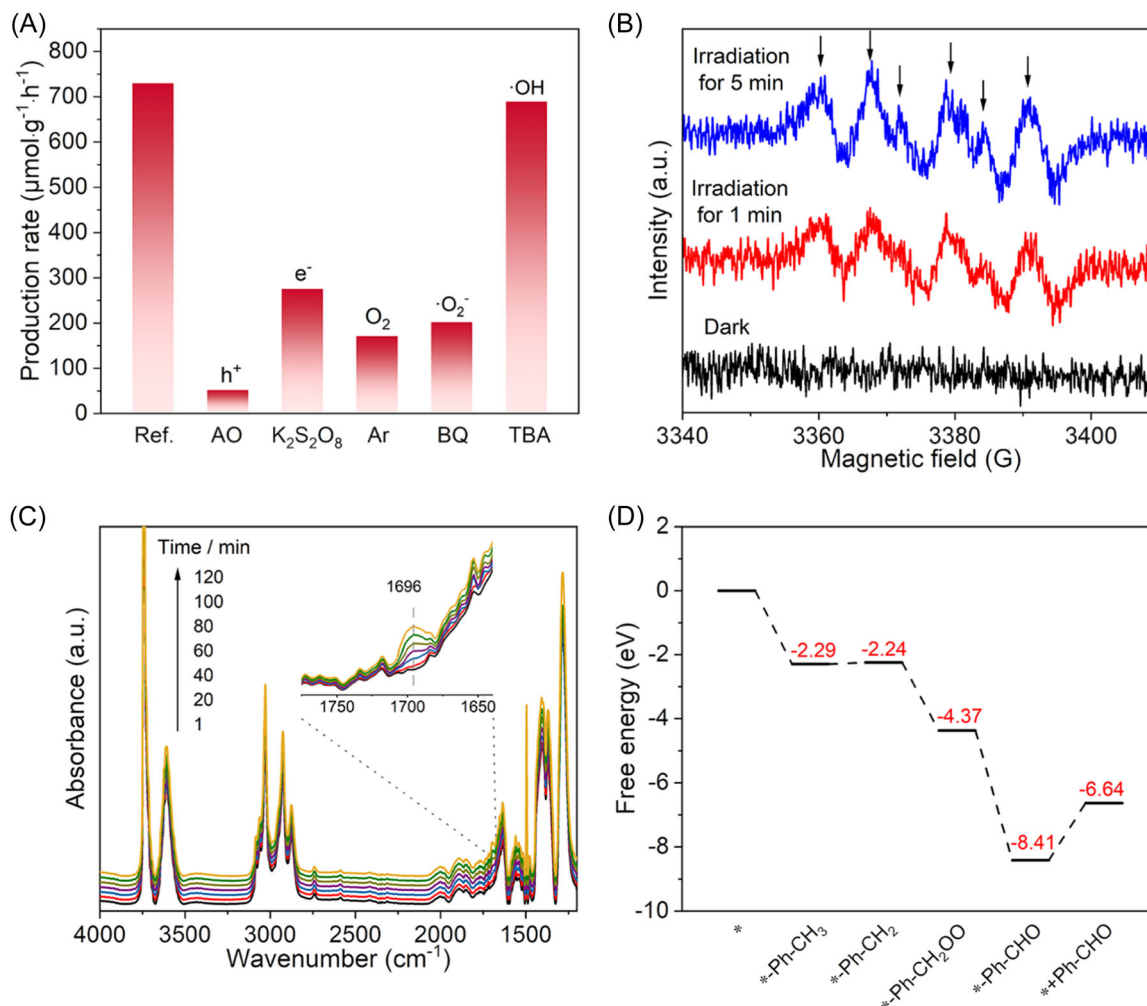**FIGURE 4** (A) The benzaldehyde production of CsPbBr$_3$@SBA-16 in the anaerobic condition or in the presence of different radical scavengers, such as AO, K$_2$S$_2$O$_8$, BQ, and TBA. Note: the LOD and the LOQ of GC for BAD are 0.04 and 0.12 μmol mL^{-1}, respectively. The mass of produced BAD with AO as the scavenger of h$^+$ falls between the LOD and LOQ of GC. Therefore, the provided value is for reference only. (B) In situ ESR spectra of superoxide radicals trapped by DMPO over CsPbBr$_3$@SBA-16 after 1 min irradiation and 5 min irradiation (arrows mark the DMPO-•O$_2^-$ peaks). (C) In situ DRIFT spectra of CsPbBr$_3$@SBA-16 in the presence of toluene and O$_2$ mixture. Inset is the focused band in the range from 1775 to 1640 cm^{-1}, and the dotted line at 1696 cm^{-1} indicates the presence of the carbonyl group. (D) Gibbs free energy diagrams of the selective photocatalytic toluene oxidation to benzaldehyde for CsPbBr$_3$ QDs.

oxidants in the photocatalytic selective oxidation of toluene over CsPbBr$_3$@SBA-16 under visible light irradiation. It is noteworthy that in the presence of K$_2$S$_2$O$_8$, under Ar atmosphere, or with BQ, the yields of BAD were comparable and higher than those with the h$^+$ scavenger, AO. This suggests that the photocatalytic oxidation of toluene is predominantly driven by photogenerated holes, with electrons (e$^-$), O$_2$, and •O$_2^-$ also participating in this oxidation reaction. Conversely, the addition of TBA as a scavenger for •OH radicals resulted in almost no change in toluene conversion, indicating that hydroxyl radicals are not relevant to this reaction system. To directly ascertain the involvement of radicals in the photocatalytic reaction, in situ electron spin resonance (ESR) experiments were conducted under

solar light irradiation, utilizing 5,5-dimethyl-1-pyrroline N-oxide (DMPO) as the trapping agent. As depicted in Figure 4B, in the absence of light irradiation, no discernible signals were observed. However, upon exposure to light, ESR signals corresponding to superoxide radicals (DMPO-•O$_2^-$) emerged in the reaction system. This observation indicates that the photogenerated electrons in CsPbBr$_3$ can reduce O$_2$ to form •O$_2^-$. Furthermore, with an extension of irradiation time, the intensities of the •O$_2^-$ peaks exhibited an increase.

In addition, we conducted in situ diffuse reflectance infrared Fourier transform spectroscopy (DRIFTS) experiments to confirm the reaction intermediates during the toluene oxidation process upon light irradiation. As shown in Figure 4C, a distinct peak corresponding to

the carbonyl group of BAD at 1696 cm^{-1} was detected. This peak gradually increased in intensity with the prolonged visible light irradiation time of the CsPbBr$_3$@SBA-16 photocatalyst. In contrast, no discernible peaks associated with benzyl alcohol were observed throughout the entire irradiation process. This observation substantiates that the formation of BAD occurs through direct oxidation of toluene, excluding benzyl alcohol as an intermediate.[22] Moreover, we conducted density functional theory (DFT) calculations to delve into the mechanism of photocatalytic C(sp^3)–H bond activation. The comprehensive results are illustrated in Figure 4D, and the interaction models of CsPbBr$_3$ QDs with each intermediate in the photocatalytic process are depicted in Figure S21. Notably, the Gibbs free energy barrier (ΔG) for toluene absorption on CsPbBr$_3$ was calculated to be negative, indicating the spontaneity of this process. Additionally, the energy barrier for C–H activation and the subsequent formation of *Ph-CH$_2$ from *Ph-CH$_3$ was determined to be +0.05 eV. This signifies that CsPbBr$_3$ substantially reduces the activation energy of the C(sp^3)–H bond. In the presence of superoxide radicals, *Ph-CH$_2$ undergoes conversion to *Ph-CH$_2$OO, followed by desorption of an OH group to form *Ph-CHO. Importantly, the generation of these intermediates over CsPbBr$_3$ exhibits negative barriers, further enhancing the efficiency of toluene oxidation. Note that the desorption of *Ph-CHO is the rate-determining step of the reaction with an energy barrier of +1.77 eV.

Through a comprehensive investigation employing active species experiments, ESR, in situ DRIFTs, and DFT calculations, a plausible hypothesis for the reaction mechanism can be proposed. Under solar light irradiation, photoinduced electrons and holes are generated in the conduction band minimum and valence band maximum of CsPbBr$_3$, respectively. The electrons undergo a reaction with O$_2$, leading to the generation of •O$_2^-$. Simultaneously, the holes engage in a reaction with toluene, forming toluene radicals—a key step in the oxidation of toluene. Eventually, these toluene radicals further react with the generated •O$_2^-$ to yield the final product, BAD.

Upon storage in ambient conditions (store open under room-temperature and humid condition), the CsPbBr$_3$@SBA-16 presents good stability as well. After 2 days and 2 months, the CsPbBr$_3$@SBA-16 sample was found to retain the same PL at 507 nm (Figures 5A and S22) indicative of the preservation of PQD size. In contrast, the emission peak of CsPbBr$_3$@MCM-41 rapidly shifted from 460 to 470 nm and 516 nm after being stored in ambient environment for 2 days and 2 months, respectively. The peak shifts were caused by the size change of CsPbBr$_3$. As shown in Figure S23, the XRD peaks attributed to CsPbBr$_3$ were still absent in CsPbBr$_3$@SBA-16 but observed in CsPbBr$_3$@MCM-41 after long storage. Meanwhile, the CsPbBr$_3$ QDs were still in the cavities of SBA-16, while CsPbBr$_3$ nanoparticles with a dimension of hundreds of nanometers were observed in the case of MCM-41 after 2 months of storage, as revealed by HAADF-STEM in Figure 5B,C. These findings indicate that the CsPbBr$_3$ QDs do not leach out from the 3D cavities but rather from the 1D channels and aggregate to form bulk CsPbBr$_3$. Moreover, after storage in the dark, ambient conditions for 2 months, the chemical states and photoactivity of CsPbBr$_3$@SBA-16 remained constant (Figures S24 and S25). These findings highlight the stability of the CsPbBr$_3$@SBA-16 sample. The improvement in the stability of PQDs highlights the strong confinement effect of the 3D cavity in SBA-16.
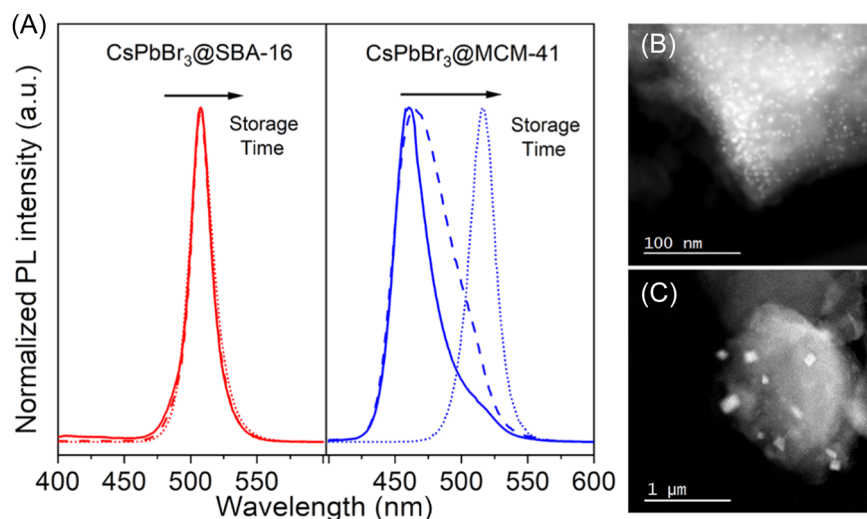

FIGURE 5 (A) PL spectra of CsPbBr$_3$@SBA-16 and CsPbBr$_3$@MCM-41 after storage under ambient conditions for 0 day (solid lines), 2 days (dash lines), and 2 months (dot lines). HAADF-STEM images of (B) CsPbBr$_3$@SBA-16 and (C) CsPbBr$_3$@MCM-41 after 2 months of long storage under ambient conditions.

CONCLUSION

In summary, we developed a TSDS approach to synthesize and encapsulate MHP QDs in the 3D cavity template material SBA-16. Due to the quantum confinement of the 3D cavity, the CsPbBr$_3$@SBA-16 exhibited a strong luminescence with 40% PLQY and an ultra-narrow FWHM of 18 nm (0.087 eV). Impressively, the CsPbBr$_3$@SBA-16 presented high photoactivity for visible-light-driven photocatalytic toluene C(sp^3)–H bond activation to produce BAD with ~730 μmol g^{-1} h^{-1} yield rate and near-unity selectivity. Most importantly, the confinement of CsPbBr$_3$ QDs in 3D cavities showed significant improvement in their stability under ambient conditions and during photocatalytic reactions, compared to both ligand-contained CsPbBr$_3$ QDs and those confined in 1D channels of MCM-41. Overall, this study provides an important approach for the future designing and synthesizing of stable MHP QDs.

CONFLICT OF INTEREST STATEMENT

The authors declare that there are no conflicts of interest.

ORCID

Yu-Jie Gao https://orcid.org/0000-0002-8216-1291
Daniel A. Esteban https://orcid.org/0000-0002-5626-9848
Bo Weng http://orcid.org/0000-0001-8337-219X
Rafikul A. Saha https://orcid.org/0000-0002-9651-6938
Min-Quan Yang https://orcid.org/0000-0001-7419-5240
Sara Bals https://orcid.org/0000-0002-4249-8017
Julian A. Steele https://orcid.org/0000-0001-7982-4413
Maarten B. J. Roeffaers https://orcid.org/0000-0001-6582-6514

REFERENCES

1. Li F, Tian D, Fan Y, et al. Chiral acid-catalysed enantioselective C–H functionalization of toluene and its derivatives driven by visible light. *Nat Commun.* 2019;10(1):1774.
2. Dai Y, Poidevin C, Ochoa-Hernández C, Auer AA, Tüysüz H. A supported bismuth halide perovskite photocatalyst for selective aliphatic and aromatic C–H bond activation. *Angew Chem Int Ed.* 2020;59(14):5788-5796.
3. Wei Y, Cheng Z, Lin J. An overview on enhancing the stability of lead halide perovskite quantum dots and their applications in phosphor-converted LEDs. *Chem Soc Rev.* 2019;48(1):310-350.
4. Chun JY, Kim BG, Kim JY, Jang W, Wang DH. Passivation engineering via silica-encapsulated quantum dots for highly sensitive photodetection. *Carbon Energy.* 2023;5(9):e350.
5. Huang H, Verhaeghe D, Weng B, et al. Metal halide perovskite based heterojunction photocatalysts. *Angew Chem Int Ed.* 2022;134:e202203261.
6. Huang H, Pradhan B, Hofkens J, Roeffaers MBJ, Steele JA. Solar-driven metal halide perovskite photocatalysis: design, stability, and performance. *ACS Energy Lett.* 2020;5(4):1107-1123.
7. Cui Z, Wang P, Wu Y, et al. Space-confined growth of lead-free halide perovskite Cs$_3$Bi$_2$Br$_9$ in MCM-41 molecular sieve as an efficient photocatalyst for CO$_2$ reduction at the gas-solid condition under visible light. *Appl Catal B.* 2022;310:121375.
8. Xu Y-F, Yang M-Z, Chen B-X, et al. A CsPbBr$_3$ perovskite quantum dot/graphene oxide composite for photocatalytic CO$_2$ reduction. *J Am Chem Soc.* 2017;139(16):5660-5663.
9. Chen T, Weng B, Lu S, et al. Photocatalytic anaerobic dehydrogenation of alcohols over metal halide perovskites: a new acid-free scheme for H$_2$ production. *J Phys Chem Lett.* 2022;13(28):6559-6565.
10. Chen K, Deng X, Dodekatos G, Tüysüz H. Photocatalytic polymerization of 3, 4-ethylenedioxythiophene over cesium lead iodide perovskite quantum dots. *J Am Chem Soc.* 2017;139(35):12267-12273.
11. Lv W, Li L, Xu M, et al. Improving the stability of metal halide perovskite quantum dots by encapsulation. *Adv Mater.* 2019;31(28):1900682.
12. Zhang Z, Li D, Dong Z, et al. Lead-free Cs$_2$AgBiBr$_6$ nanocrystals confined in MCM-48 mesoporous molecular sieve for efficient photocatalytic CO$_2$ reduction. *Solar RRL.* 2023;7(9):2300038.
13. Gurung B, Pradhan S, Sharma D, et al. CsPbBr$_3$ perovskite quantum dots as a visible light photocatalyst for cyclisation of diamines and amino alcohols: an efficient approach to synthesize imidazolidines, fused-imidazolidines and oxazolidines. *Catal Sci Technol.* 2022;12(19):5891-5898.
14. Lan S, Pan B, Liu Y, et al. Preparation and promising optoelectronic applications of lead halide perovskite patterned structures: a review. *Carbon Energy.* 2023;5(10):e318.
15. Protesescu L, Yakunin S, Bodnarchuk MI, et al. Nanocrystals of cesium lead halide perovskites (CsPbX$_3$, X = Cl, Br, and I): novel optoelectronic materials showing bright emission with wide color gamut. *Nano Lett.* 2015;15(6):3692-3696.
16. Li X, Wu Y, Zhang S, et al. CsPbX$_3$ quantum dots for lighting and displays: room-temperature synthesis, photoluminescence superiorities, underlying origins and white light-emitting diodes. *Adv Funct Mater.* 2016;26(15):2435-2445.
17. Pan S, Li J, Wen Z, et al. Halide perovskite materials for photo (electro) chemical applications: dimensionality, heterojunction, and performance. *Adv Energy Mater.* 2021;12(4):2004002.
18. Shankar H, Ghosh S, Kar P. Boosting the stability of lead halide perovskite nanocrystals by metal-organic frameworks

and their applications. *J Mater Chem C*. 2022;10(32): 11532-11554.

19. Rubino A, Caliò L, García-Bennett A, Calvo ME, Míguez H. Mesoporous matrices as hosts for metal halide perovskite nanocrystals. *Adv Opt Mater*. 2020;8(9):1901868.

20. Polavarapu L, Nickel B, Feldmann J, Urban AS. Advances in quantum-confined perovskite nanocrystals for optoelectronics. *Adv Energy Mater*. 2017;7(16):1700267.

21. Wang HC, Lin SY, Tang AC, et al. Mesoporous silica particles integrated with all-inorganic $CsPbBr_3$ perovskite quantum-dot nanocomposites (MP-PQDs) with high stability and wide color gamut used for backlight display. *Angew Chem Int Ed*. 2016;55(28):7924-7929.

22. Yu X, Wu L, Yang D, et al. Hydrochromic $CsPbBr_3$ nanocrystals for anti-counterfeiting. *Angew Chem Int Ed*. 2020;59(34):14527-14532.

23. Zhang Q, Zheng W, Wan Q, et al. Confined synthesis of stable and uniform $CsPbBr_3$ nanocrystals with high quantum yield up to 90% by high temperature solid-state reaction. *Adv Opt Mater*. 2021;9(11):2002130.

24. Dirin DN, Protesescu L, Trummer D, et al. Harnessing defect-tolerance at the nanoscale: highly luminescent lead halide perovskite nanocrystals in mesoporous silica matrixes. *Nano Lett*. 2016;16(9):5866-5874.

25. Malgras V, Tominaka S, Ryan JW, et al. Observation of quantum confinement in monodisperse methylammonium lead halide perovskite nanocrystals embedded in mesoporous silica. *J Am Chem Soc*. 2016;138(42):13874-13881.

26. Zhang Q, Sun X, Zheng W, et al. Band gap engineering toward wavelength tunable $CsPbBr_3$ nanocrystals for achieving rec. 2020 displays. *Chem Mater*. 2021;33(10):3575-3584.

27. Song W, Liu L, Zhou W, Zhang J, Yu L, Lian S. One-step melt closed mesoporous SiO_2 for large-scale synthesis of confined $CsPbX_3$ (X = Cl, Br, and I) quantum dots and LED applications. *ACS Appl Nano Mater*. 2022;5(8):11549-11558.

28. Duan Y, Wang DY, Costa RD. Recent progress on synthesis, characterization, and applications of metal halide perovskites@metal oxide. *Adv Funct Mater*. 2021; 31(49):2104634.

29. Budi CS, Deka JR, Saikia D, Kao H-M, Yang Y-C. Ultrafine bimetallic Ag-doped Ni nanoparticles embedded in cage-type mesoporous silica SBA-16 as superior catalysts for conversion of toxic nitroaromatic compounds. *J Hazard Mater*. 2020;384:121270.

30. Wang C, Huang H, Weng B, et al. Planar heterojunction boosts solar-driven photocatalytic performance and stability of halide perovskite solar photocatalyst cell. *Appl Catal B*. 2022;301:120760.

31. Brennan MC, Zinna J, Kuno M. Existence of a size-dependent stokes shift in $CsPbBr_3$ perovskite nanocrystals. *ACS Energy Lett*. 2017;2(7):1487-1488.

32. Wang P, Wang B, Liu Y, et al. Ultrastable perovskite–zeolite composite enabled by encapsulation and in situ passivation. *Angew Chem*. 2020;132(51):23300-23306.

33. Guo X-X, Tang S-F, Mu Y-F, Wu L-Y, Dong G-X, Zhang M. Engineering a $CsPbBr_3$-based nanocomposite for efficient photocatalytic CO_2 reduction: improved charge separation concomitant with increased activity sites. *RSC Adv*. 2019;9(59):34342-34348.

34. Huang H, Yuan H, Zhao J, et al. $C(sp^3)$–H bond activation by perovskite solar photocatalyst cell. *ACS Energy Lett*. 2019;4(1): 203-208.

35. Deng J, Xu D, Zhang J, et al. $Cs_3Bi_2Br_9$/BiOBr S-scheme heterojunction for selective oxidation of benzylic C−H bonds. *J Mater Sci Technol*. 2024;180:150-159.

36. Deng J, Lei W, Fu J, Jin H, Xu Q, Wang S. Enhanced selective photooxidation of toluene to benzaldehyde over Co_3O_4-modified BiOBr/AgBr S-scheme heterojunction. *Solar PRL*. 2022;6(8):2200279.

SUPPORTING INFORMATION

Additional supporting information can be found online in the Supporting Information section at the end of this article.